



Proofreading and single-molecule sensitivity in T cell receptor signaling by condensate nucleation

William L. White^{a,b} , Hailemikael K. Yirdaw^a, Ariel J. Ben-Sasson^b , Jay T. Groves^{c,d} , David Baker^{b,e,f} , and Hao Yuan Kueh^{a,g,1}

Affiliations are included on p. 10.

Edited by Ronald Vale, Howard Hughes Medical Institute, Ashburn, VA; received December 3, 2024; accepted April 23, 2025

T cells display the remarkable ability to detect single foreign peptides displayed on target cells, while ignoring highly abundant self-peptides. This selectivity has been explained by kinetic proofreading in the T cell receptor (TCR) signaling pathway, which prevents responses to short-lived binding events regardless of their abundance. However, the biochemical mechanisms that drive kinetic proofreading have remained unclear. Here, using computational modeling, we show that these key signaling properties of the TCR pathway can emerge from the dynamics of linker for activation of T cells (LAT) phosphorylation, diffusion, and condensation following TCR-peptide major histocompatibility complex (pMHC) binding. In this model, time delays in LAT condensate nucleation underlie kinetic proofreading, enabling selective signaling responses to high-affinity pMHC ligands. The cooperativity in the nucleation and growth of LAT condensates also provides a mechanism to amplify weak signals from single high-affinity peptides and for condensates to grow with increasing antigen numbers. In contrast to other models, condensate-nucleation proofreading predicts a dependence of signal strength on pMHC spacing at fixed number, a prediction we validated experimentally using a protein scaffold to present pMHCs at defined intervals. Our results suggest that nucleation-condensation proofreading underlies the remarkable antigen detection capabilities of the TCR signaling pathway.

T cell receptor signaling | phase separation | nucleation-condensation | kinetic proofreading | stochastic computational modeling

The T cell receptor (TCR) signaling pathway simultaneously achieves several functional properties that enable T cells to sense and appropriately respond to challenges of varying types and severities (1). First, it senses foreign peptide antigens displayed as peptide major histocompatibility complexes (pMHCs) in a highly sensitive manner, in some cases detecting single foreign pMHCs (2). Second, it is highly selective so as to avoid responding to more abundant self-antigens, which have a weaker TCR binding affinity (3, 4). And finally, although the TCR signaling pathway activates in an all-or-none manner upon pMHC recognition (5–7), it can also tune its response to different antigen levels in an analog manner, enabling T cells to tailor their responses to the magnitude of the threat (8, 9). Despite significant advances in our knowledge of the biochemistry of TCR signaling (10, 11), it remains incompletely understood how this pathway is able to simultaneously achieve sensitivity, selectivity, and dynamic range in antigen sensing.

The first step in T cell activation after a pMHC binds to the TCR is phosphorylation of the TCR complex by the kinase Lck(10), leading to activation of the kinase ZAP70 (12). Next, ZAP70 phosphorylates several key proteins, including the transmembrane protein linker for activation of T cells (LAT) (10), leading to T cell activation. To explain how these steps can generate selective responses to foreign peptides based on their stronger binding affinity, the concept of kinetic proofreading has been proposed (13) and extensively studied using mathematical modeling (3, 5, 8, 14–16). In its most basic form, kinetic proofreading consists of a series of biochemical steps that can occur only when a TCR is bound to a pMHC, and that are quickly reversed when the pMHC unbinds (13). This allows the T cell to respond strongly to foreign antigens that bind long enough to complete all necessary steps, while ignoring self-antigens, which bind only briefly.

A number of extensions of the basic kinetic proofreading model have been evaluated, and shown to improve different facets of the signaling behavior. The addition of a negative feedback loop can dramatically enhance signaling selectivity (3), whereas positive feedback loops can enhance sensitivity to low pMHC copy numbers (5, 17), generating an all-or-none “digital” response. On the other hand, incoherent feedforward loops can expand the dynamic range of the T cell response (8). However, while these changes to feedback circuit topologies can improve one individual facet of circuit function, they often

Significance

To fight infections and cancer, T cells must selectively recognize low levels of foreign peptides from pathogens or cancer cells, but the mechanisms that enable these properties remain unclear. Using computational modeling and experiments, we find that T cells can selectively detect single foreign peptides through a clustering process where key proteins downstream of the T cell receptor form condensates containing hundreds of signaling proteins. This condensate nucleation process explains experimentally observed features of T cell signaling, including our finding that the size of signaling clusters depends on the distance between foreign peptides. Our work reveals a key role for the condensation of signaling molecules in setting spatial and temporal thresholds that control the sensitivity and selectivity of T cells.

Author contributions: W.L.W., J.T.G., and H.Y.K. designed research; W.L.W. and H.K.Y. performed research; A.J.B.-S. and D.B. contributed new reagents/analytic tools; W.L.W. and H.K.Y. analyzed data; J.T.G. edited the paper; and W.L.W. and H.Y.K. wrote the paper.

The authors declare no competing interest.

This article is a PNAS Direct Submission.

Copyright © 2025 the Author(s). Published by PNAS. This article is distributed under [Creative Commons Attribution-NonCommercial-NoDerivatives License 4.0 \(CC BY-NC-ND\)](https://creativecommons.org/licenses/by-nc-nd/4.0/).

¹To whom correspondence may be addressed. Email: kueh@uw.edu.

This article contains supporting information online at <https://www.pnas.org/lookup/suppl/doi:10.1073/pnas.2422787122/-/DCSupplemental>.

Published May 30, 2025.

do so at the expense of another. Strong positive feedback can significantly improve the sensitivity of a signaling pathway, but can create a digital system that is either “on” or “off” and lacks dynamic range (5, 18). Conversely, negative feedback can improve selectivity, at the expense of sensitivity to low ligand levels (5, 18). Additionally, T cells need to sense antigens at very low copy numbers, where stochastic effects can dominate (16, 19, 20). It is therefore unclear how a single signaling pathway can balance the competing demands of selectivity, sensitivity, and dynamic range, especially in a stochastic regime.

The clustering of signaling molecules downstream of the TCR could help explain these cardinal properties of T cell signaling. Pioneering studies from Su and co-workers established that LAT can undergo condensation and phase separation when phosphorylated (21, 22), as predicted by earlier studies (23). Phospho-tyrosine (pY) sites on phospho-LAT (pLAT) act as binding sites for Grb2 and PLC γ , among other proteins (21, 22). Both Grb2 and PLC γ contain additional domains that can bind to several sites on son of sevenless (SOS) (21, 22, 24). This network of polyvalent interactions causes these molecules to form condensates tethered to the membrane by LAT (21, 22, 24), and recruits other molecules which, together with PLC γ and SOS, transmit the activation signal into the T cell (10, 25). Some computational modeling work has begun to explore LAT condensation with Grb2, SOS, and PLC γ using coarse-grained molecular dynamics simulations (22, 26). However, these studies focus on condensate formation and growth within a steady-state context and not its role in the dynamics of signaling initiation. The experimental evidence for the importance of LAT clustering in TCR signaling (21, 22, 24, 27) motivates the need to create models that include this biophysical process and to investigate its relationship to key signaling properties.

To address this gap, we developed a computational model to study the dynamics of LAT condensation driven by TCR signaling. In this model, TCR antigen engagement leads to localized LAT phosphorylation and condensation at the cell membrane. This model displays all critical signaling properties of the TCR pathway, including its sensitivity to low ligand numbers, selectivity to high affinity ligands, and dynamic range in response to variations in pMHC numbers. We also compare our model to experimental results, including clustering dynamics in response to single pMHC–TCR binding events (27). Finally, we experimentally validate our model’s spatial predictions using a designed protein system (28) that allows independent variation of antigen spacing and number. These findings establish a quantitative framework for understanding T cell threat sensing and discrimination.

Results

The LAT Condensation Model. To assess the contribution of LAT condensation to TCR signaling we built a dynamical model of the diffusion and clustering of LAT at the membrane. To capture these behaviors we built our model on a two dimensional (2D) grid representing the plasma membrane of a T cell. Within this grid, we model the location of TCRs and LAT molecules, both of which can diffuse freely in the membrane (Fig. 1B). Other signaling- and condensation-related molecules such as ZAP70, SOS, Grb2, PLC γ , and CD45 are modeled implicitly by the effects they have on either TCRs or LAT molecules. In each time-step of a simulated signaling trajectory, the actions of each TCR and LAT molecule are chosen independently and stochastically, based on each molecule’s context, and the simulation grid is updated accordingly. By explicitly modeling the location of each molecule

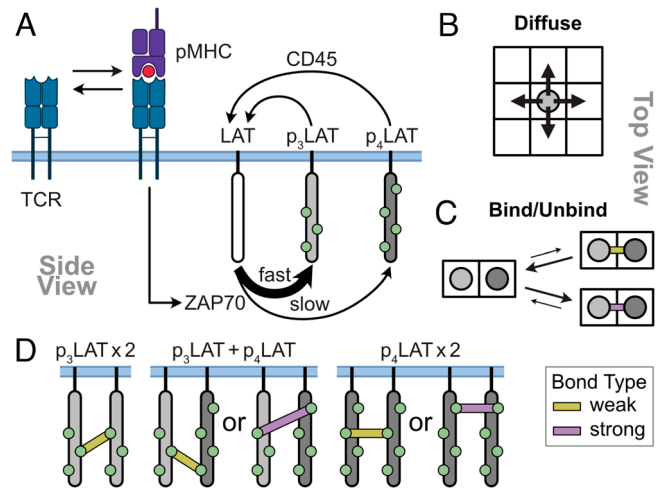


Fig. 1. Model for TCR signaling by LAT condensation. (A) In this model, pMHC binding to the TCR triggers local LAT phosphorylation through rapid activation of downstream enzymes (e.g., Lck and ZAP70). Phosphorylation produces p₃LAT (light gray), phosphorylated at Y171, Y191, and Y226; and p₄LAT (dark gray), additionally phosphorylated at Y132. pLAT is dephosphorylated (e.g., by CD45). (B) pLAT molecules diffuse on a 2D grid. (C) Adjacent pLAT molecules bind to each other via cross-linking molecules not explicitly modeled. Bonds are either weak (yellow bar; slow on-rate, fast off-rate) or strong (purple bar; fast on-rate, slow off-rate). (D) Strong bonds (purple bars) require that at least one of the bonded pLAT molecules be p₄LAT; weak bonds (yellow bars) involve either p₃LAT or p₄LAT.

our model can capture signaling effects that occur due to spatial inhomogeneities not considered in existing models.

To interrogate the role of LAT condensation independently from other signaling steps, we omit the phosphorylation steps between TCR binding and ZAP70 activation. Instead, we assume that a pMHC-bound TCR immediately initiates LAT phosphorylation in its local neighborhood (Fig. 1A). This assumption is based on findings that LAT phosphorylation is a rate-limiting step for T cell signaling initiation (29, 30), suggesting that the earlier steps occur on a faster timescale. In reality, upstream events do take time to occur, and are likely also involved in kinetic proofreading (31, 32), especially in suppression of signals from very short binding ligands (less than a second). We chose to leave out the effects of earlier phosphorylation steps in order to isolate LAT condensation, and evaluate the degree to which it contributes to kinetic proofreading and other signaling properties.

A pMHC-bound TCR continues fueling LAT phosphorylation either until the pMHC dissociates, or the TCR is inactivated. TCR inactivation, though not completely understood, is in line with experimental observations (27), and could involve negative feedback through phosphatases or TCR trafficking within the immune synapse. To simplify our model, we assume that TCR inactivation occurs independently for individual TCRs with first-order kinetics.

We assume that the active pMHC–TCR complex phosphorylates LAT at four pY sites (33): Three sites are phosphorylated at a higher rate, while one (Y132) is a less ideal ZAP70 substrate and is phosphorylated at a lower rate (29, 34) (Fig. 1A). We model the Y132 site separately from the other sites, as its slower phosphorylation has been shown to be a rate limiting step in T cell signal initiation (29, 30). Accordingly, our model contains two types of pLAT: p₄LAT, which has all pY sites phosphorylated and can participate in PLC γ -mediated bonds, and p₃LAT, which has no phosphorylation on Y132 and can bind other p₃LAT only via weaker Grb2–SOS-mediated interactions (Fig. 1A, C, and D). These reversible interactions are multivalent and allow LAT to form a condensate by creating a network of bonds through its pY sites (10, 11, 21).

pLAT condensate formation is opposed by the activity of phosphatases (such as CD45) which dephosphorylate pLAT, rendering it incapable of crosslinking (Fig. 1A) (35, 36). While phosphatases act rapidly at uncondensed LAT sites, steric hindrance and exclusion from condensates limit their activity on clustered pLAT (21, 22, 37). We thus modeled a slower dephosphorylation rate for pLAT that has more bonds to other pLAT, with the stronger binding of PLC γ to pY132 offering a higher degree of protection than the weaker Grb2/SOS mediated bonds.

Altogether, our model captures the key physical and chemical processes underlying TCR-induced LAT clustering, thus allowing us to assess how this emergent phenomenon contributes to the observed characteristics of the TCR signaling pathway.

Phosphorylated LAT Condenses Above a Critical Concentration.

In vitro studies have shown that pLAT can undergo phase separation above a critical concentration (21). To determine whether our model could recapitulate similar pLAT condensation behavior we ran simulations where the number of pLAT molecules was held constant. In these simulations, we expect to observe behaviors that resemble a phase transition, including the presence of a critical concentration below which clusters do not form, and above which they form rapidly (38, 39). Consistent with these expectations, we observed a sharp transition where pLAT began to form clusters above the critical concentration ($27 \mu\text{m}^{-2}$; *SI Appendix, Fig. S1 A–C* and *Movies S1* and *S2*). Finally, we found that the mean time to first cluster decreases with concentration following a power law with an exponent of 2.99 ± 0.17 , suggesting that cluster nucleation requires simultaneous binding of three pLAT molecules (*SI Appendix, Fig. S1D*). These results demonstrate that the model recapitulates the sharp, all-or-none nature of nucleation and condensation as intended and allows us to explore how these features can contribute to the behaviors of the TCR signaling pathway as a whole.

Individual Bound TCRs Nucleate Signaling Condensates with a Time Delay. Having shown that pLAT alone can form clusters above a critical concentration in our model, we proceeded to ask whether pLAT can form clusters in response to TCR–pMHC engagement. Single-molecule studies have previously shown that individual TCRs can induce LAT clusters with a variable time delay after pMHC binding (27). In these experiments TCRs are only tracked after they bind to a pMHC, and the pMHCs used are very high affinity. To mimic these experiments, we ran our simulations with the TCR constantly bound to pMHC throughout the simulation (Fig. 2A and B).

From simulations, we found that single active TCRs can nucleate clusters of pLAT molecules with a time delay, consistent with experimental observations (27) (Fig. 2A and *Movie S3*). In these representative simulations (Fig. 2) we found that a small cloud of pLAT molecules formed under the active TCR very shortly after the start of the simulation. While pLAT molecules in this cloud could interact with one another, these interactions were transient, such that the majority of molecules were either monomers or dimers (Fig. 2C; 0 to 15 s). However, in one simulation, there was an abrupt transition after a time delay, where a pLAT cluster became nucleated and proceeded to grow rapidly, giving rise to a large cluster (Fig. 2C; upper trace, 20 to 45 s). Once formed, the cluster began to dissipate after the TCR was deactivated (Fig. 2C; upper trace, 70 to 120 s).

Across simulations, LAT clustering was all-or-none and probabilistic in nature: While every active TCR gave rise to a cloud of pLAT monomers, some gave rise to LAT clusters, while others did not (Fig. 2B and *Movie S4*). Notably, these results show that a single pMHC ligand can give rise to a large cluster containing

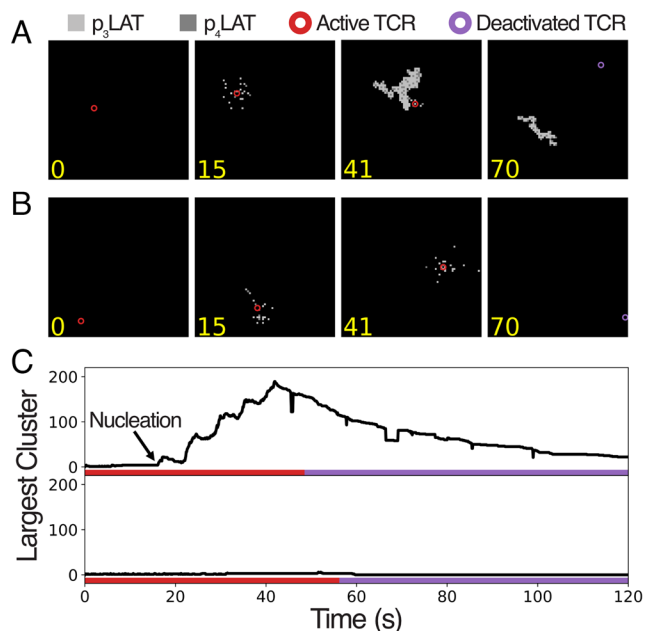


Fig. 2. Individual bound TCRs nucleate LAT condensates with a time delay. (A and B) Snapshots from two example simulations of single permanently bound TCRs. Gray squares represent p₃LAT (light) and p₄LAT (dark). Circles represent active (red) and deactivate (purple) TCRs. Each snapshot represents a $2.25 \times 2.25 \mu\text{m}$ square. Timestamps in seconds. (C) Trace of largest cluster size over time in the same simulations, with the cluster nucleation event marked. The colored bar indicates whether the TCR is active (red) or inactive (purple).

hundreds of LAT molecules. This remarkable amplification in the number of active signaling molecules is also observed experimentally (15, 27) and demonstrates the ability of a condensation-based signaling system to sensitively amplify signals from single molecule binding events.

Simulated LAT Cluster Sizes and Dynamics Match Single-Molecule Imaging. To further validate our model, we compared LAT clustering dynamics from simulations to those previously seen in single-molecule imaging experiments (27) (Fig. 3). These experiments track individual pMHC–TCR complexes and LAT clusters that form nearby and allow delay times and size distributions of pLAT clusters to be precisely measured.

We first quantified the delay time between pMHC binding and pLAT cluster formation (τ_{clust} ; Fig. 3A and B) because this time delay in LAT nucleation could constitute a kinetic proofreading step. Nucleation times were quantified as the time at which the number of LAT molecules reached a fixed threshold; however, we note that our results do not depend qualitatively on the threshold. Alternative cutoffs (*SI Appendix, Fig. S2 A and C*) or even alternative definitions of clustering (*SI Appendix, Fig. S2 B, D, and E*) show similarly shaped τ_{clust} distributions, suggesting that clustering does occur with a delay, regardless of our definition of a cluster. Comparing the simulated and experimental distributions, we find that they are strikingly similar with an initial rise peaking around 15 to 20 s, followed by a slow decay (Fig. 3B) (27). Critically, both distributions do not follow a monotonic decay as expected from a first-order process. This delay in LAT cluster nucleation could contribute to selectivity by filtering out short-lived binding events from weak ligands, a possibility we will test below.

We next compared LAT cluster sizes obtained from simulation to those measured in single-molecule imaging experiments, specifically comparing the maximal number of pLAT molecules in clusters, N_{max} , over the course of a simulation to the number of pLAT molecules in experimentally observable clusters (Fig. 3A).

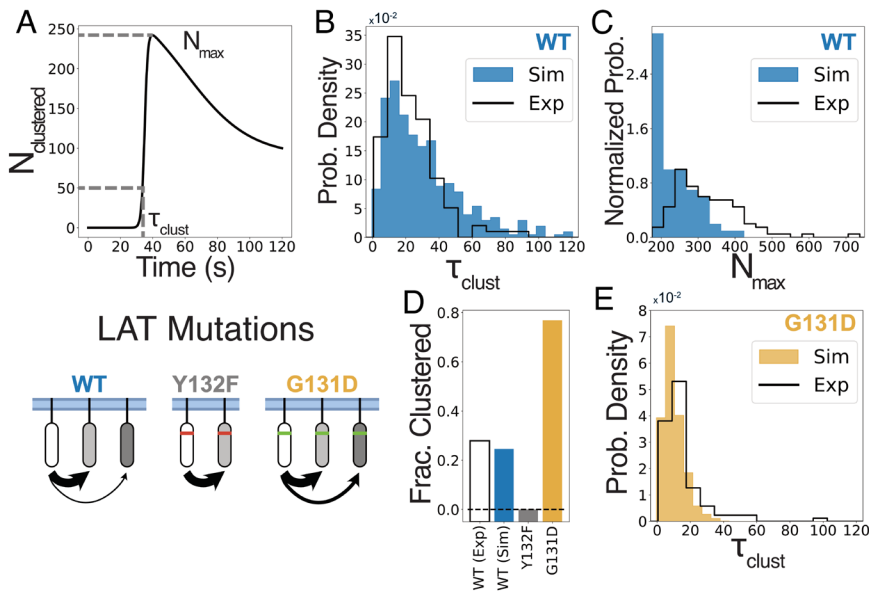


Fig. 3. LAT condensates nucleate with a time delay that is shortened by enhanced Y132 phosphorylation, in agreement with experimental results. Data from simulations of single permanently bound TCRs on cells with varying LAT mutations. 1,500 replicate simulations were run for each mutant. (A) Example trace showing the number of clustered pLAT molecules. N_{\max} denotes the maximum number of clustered molecules over the simulation. τ_{clust} denotes the time at which the first cluster of size 50 or greater is formed. (B) Distribution of τ_{clust} values in simulations for WT LAT (blue bars) or compared to the experimental distribution (27) (black line). Simulations with no clusters are omitted from these distributions. (C) Distribution of N_{\max} over replicate simulations with WT LAT (blue bars) compared to the experimentally determined distribution (27) (black line). Simulated distribution is truncated at the lowest observable cluster size and both distributions are normalized to facilitate comparison. (D) Bar chart showing the fraction of simulations producing a LAT cluster for various LAT mutants (colored bars) compared to the experimentally determined value for WT LAT (27) (black outline). (E) Distribution of τ_{clust} values as in (B) for G131D LAT (yellow bars) compared to the experimental distribution (27) (black line).

We note that, because small LAT clusters are below the limit of detection in experiments, the experimental cluster size distribution would not include many of the small clusters present in our simulations. Thus, we compared LAT cluster sizes above roughly 200 molecules. Our simulations show a range of N_{\max} values up to about 450 molecules (Fig. 3C and *SI Appendix, Fig. S3A*), slightly smaller than the largest experimentally observed clusters (27). Thus, in our model, single TCR binding events can give rise to clusters containing hundreds of LAT molecules, similar in size to those observed experimentally.

Finally, in single-molecule experiments, pMHC-bound TCRs gave rise to pLAT clusters only in a fraction of cases (25 to 50%), even when they were bound for very long times (27). This cap on TCR-induced clustering likely arises from feedback mechanisms which deactivate pMHC-bound TCRs over time. As the binding lifetime increases, if a cluster has not yet formed, it becomes more likely that the TCR will be deactivated before a cluster can form. This negative feedback sets the probability of clustering at about 27% in single-molecule experiments (27) and in our simulations (Fig. 3D, WT).

The probability of forming a cluster, the size of the cluster that is formed, and the delay between pMHC–TCR binding and cluster formation are all critical parameters controlling the T cell response at a cellular and population level. The close agreement in these measurements between our simulated results and experimental data suggest that our model is able to accurately capture these key aspects of early TCR signaling.

LAT Phosphorylation Kinetics Modulate the Time Delay to Condensate Nucleation. LAT Y132 phosphorylation has been shown to be a rate-limiting step in T cell signal initiation (29), and LAT mutations that accelerate this reaction have further been shown to promote LAT cluster formation (27). Here, we tested whether changes to rates of Y132 phosphorylation can modulate time delays to condensate nucleation. We simulated two mutations in LAT which are known to affect both the PLC γ binding site and the kinetics of signaling. The G131D mutation increases the rate of ZAP70 activity at Y132 (29), which we modeled as an increase in the p_4 LAT production rate in our simulations. Conversely, the Y132F mutation completely prevents phosphorylation at the same site, modeled as a reduction of the p_4 LAT production rate to zero. We first observed that these mutations had the expected

effect on the fraction of TCR binding events that are productive. Y132F completely abolishes clustering in simulations (Fig. 3D), paralleling the dramatic reduction in signaling observed in T cells bearing that mutation (33, 40). Conversely, G131D increases the productive binding rate from 27% to about 77% (Fig. 3D), in agreement with the observation that T cells bearing this mutation are more easily activated (29).

In addition to affecting the probability of clustering, G131D dramatically reduces nucleation delay times. Both simulated and experimental results show an earlier peak in the delay time distribution and a shorter tail to the right of the distribution (Fig. 3E) (27). The shortened delay suggests a decreased ability for G131D cells to discriminate between weak and strong binding pMHCs.

Through these simulations we show that our model recapitulates the effects of mutations in LAT that affect the kinetics of its phosphorylation at the key Y132 site. We additionally show that similar results arise when we use an alternate set of parameters, or a shorter simulation time step (*SI Appendix, Fig. S3*); these results indicate that our conclusions are robust and our model is not overly dependent on our assumptions. Under both parameter sets, we are able to recapitulate expected effects on the frequency of cluster formation as well as on the distribution of cluster initiation times. More broadly, we are able to show that the kinetics of LAT phosphorylation have a direct influence on the signaling outcome, and are likely to influence kinetic proofreading via modulation of delay time distributions.

Kinetic Proofreading by Condensate Nucleation in TCR Signaling. The observed delay between pMHC binding and LAT condensation can potentially serve as a kinetic proofreading step enabling T cells to selectively respond to high-affinity pMHC ligands. To test this idea, we simulated many TCRs on a single cell stimulated with pMHCs with varying lifetimes of TCR binding. We note that our model tracks the positions of TCRs but not pMHCs, ignoring local rebinding of a pMHC to a nearby TCR, because of its low likelihood (*SI Appendix, Eqs. 14–20*). In order to allow a fair comparison between different affinity pMHCs, we increased the simulated concentration of the pMHC as its TCR binding lifetime decreased such that TCR occupancy was held constant (Fig. 4 A and C). The simulation results confirm that the concentrations were selected appropriately (Fig. 4C). Despite constant TCR occupancy, LAT clustering occurred preferentially in response to stimulation with tight-binding pMHCs,

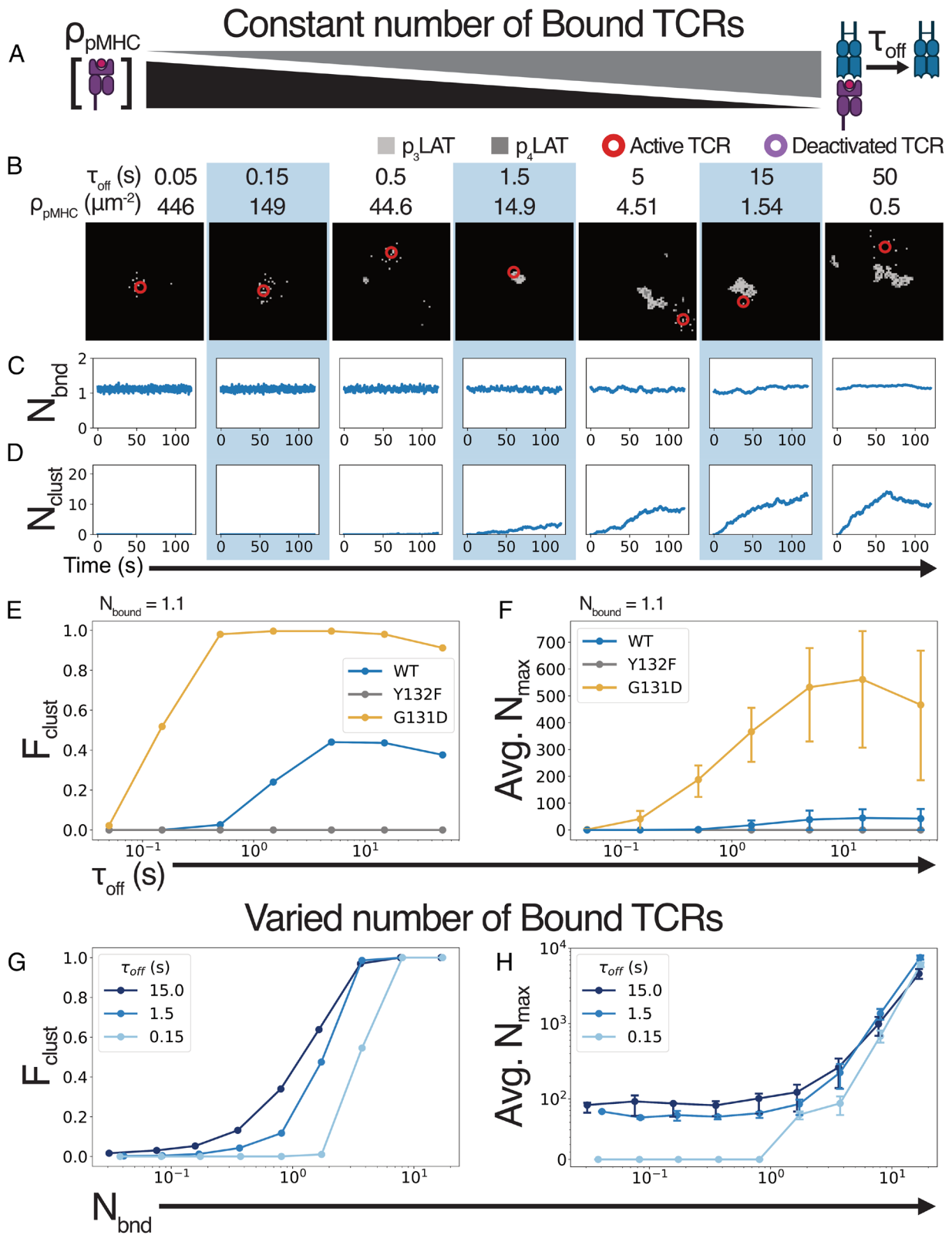


Fig. 4. Delays in pLAT condensate nucleation enable kinetic proofreading in TCR signaling. (A–F) Data from simulations of varying pMHC lifetimes and LAT mutants, with TCR occupancy held constant. 500 replicate simulations were run for each condition. (A) Schematic showing the simultaneous increase in pMHC-TCR bond lifetime and decrease of pMHC 2D density used to achieve constant numbers of bound TCRs. (B) Snapshots of representative simulations at each pMHC off-rate with WT LAT. Light gray squares represent $p_3\text{LAT}$ and dark gray represent $p_4\text{LAT}$. Circles represent bound TCRs, red for active and purple for deactivated. Each snapshot represents a $1.7 \times 1.7 \mu\text{m}^2$. (C) Average number of bound TCRs (N_{bound}) over time for simulations at each pMHC off-rate with WT LAT. (D) Average number of pLAT molecules in clusters of size 50 or greater (N_{clust}) for the same simulations in (C). (E) The fraction of simulations that produce a cluster of size 50 or greater (F_{clust}) as in B–D, the number of bound TCRs is held fixed. (F) Mean N_{max} over replicate simulations for the same simulations as in (E). Error bars show 25th and 75th percentiles of replicate simulations. (G and H) Data from simulations with varying pMHC dose and lifetime, with WT LAT. 495 replicate simulations were run per condition. (G) F_{clust} for simulations yielding varied numbers of bound TCRs at each of three TCR-pMHC half-lives. (H) The mean N_{max} in simulations where a cluster forms for the same stimulation conditions as (G). Error bars show 25th and 75th percentiles of replicate simulations. TCR occupancy (N_{bound}) is measured as the average number of bound TCRs throughout all simulations within a given condition.

with little or no clustering occurring for pMHC ligands with shorter binding lifetimes ($\tau_{\text{off}} < 0.5$ s) (Fig. 4 *B*, *D*, and *E* and [Movies S5–S11](#)). Furthermore, as pMHC binding lifetimes increased, cluster sizes and clustering likelihoods increased, indicating that the system is able to encode pMHC affinity information at this step. Because the TCR occupancies are matched across all simulations, the reduced clustering observed with the faster off-rates can only be due to a kinetic proofreading mechanism. To the extent that this occurs in these simulations, the proofreading is carried out solely by LAT condensation, and not any upstream components of the pathway since they are not considered in our model. These results directly demonstrate kinetic proofreading by LAT condensation.

To probe the role of slow LAT phosphorylation in setting time delays in kinetic proofreading, we ran the same TCR occupancy-matched simulations with the G131D and Y132F mutants and looked at the effects of these mutations on signaling magnitude and proofreading. As expected, G131D increased the LAT clustering response both in terms of probability of clustering (Fig. 4*E*) and the size of the clusters (Fig. 4*F*), while Y132F again completely prevented clustering. Strikingly, G131D drastically reduces the ability of the simulated cells to distinguish lower-affinity peptides ($\tau_{\text{off}} \leq 0.5$ s) from higher-affinity peptides ($\tau_{\text{off}} \geq 5$ s) with roughly half of G131D simulations responding to peptides with 150 ms half-lives (Fig. 4*E*). The reduced degree of proofreading caused by this mutation explains why mice bearing this mutation show enhanced responses to weak pMHC stimuli and develop autoimmune disease (30).

Together, these results indicate that LAT nucleation constitutes a key kinetic proofreading step in T cell signaling. The delay imposed by the rarity of nucleation events provides a simple mechanism for filtering out short-lived pMHC–TCR interactions. Additionally, the phosphorylation rate of the PLC γ binding site is a critical parameter that controls the threshold for binding lifetimes that are able to produce a condensation response.

Cluster Growth Allows Wide Dynamic Range. In addition to distinguishing between ligands of varying affinity, T cells may also distinguish between varying pMHC levels (9), which indicate the severity of the infection. Most current models propose that signaling is digital at the single cell level such that pMHC dose does not alter the response at the single-cell level but tunes the percentage of cells that respond (5). However, some aspects of TCR signaling have been demonstrated to respond to pMHC dose in a graded manner at the single cell level (9, 41).

To determine the extent to which LAT clustering can convey information about pMHC dose, we tested the response of our model to doses of three different antigens spanning three orders of magnitude (Fig. 4 *G* and *H*). We first tested the response at the population level and found that the fraction of simulated cells that form a large cluster increases with the antigen dose and lifetime (Fig. 4*G*). This result highlights the digital nature of clustering, and provides a clear binary signal as to whether a threat has been detected by the cell. The rightward shift of these curves as pMHC binding lifetime decreases serves as further confirmation of kinetic proofreading. Interestingly, the proofreading is strongest at low TCR occupancy, where only the strongest binding pMHC can produce any clusters. Since higher occupancies require supraphysiological pMHC levels, this result suggests that LAT condensation dynamics are tuned to maximize kinetic proofreading under naturally occurring conditions.

We next examined the response at a single cell level and found that changes in cluster size allow for an expanded dynamic range. Specifically, as the fraction of cells responding begins to saturate, the size of the cluster begins to grow (Fig. 4*H*). Therefore, even at antigen doses where all cells respond, larger doses can be

differentiated based on cluster size. Together, these results explain how LAT clustering dynamics could give rise to digital activation for signal amplification and single molecule sensitivity, as well as analog tuning for dynamic range in pMHC dose detection.

LAT Condensation Sets an Optimal pMHC Spacing for T Cell Activation. The analysis above shows that our LAT condensate nucleation model can uniquely give rise to sensitivity, specificity, and dynamic range in TCR signaling. This model agrees with existing experimental data; however, we have not yet shown how our model can be distinguished from other existing kinetic proofreading models. Most other dynamic models assume a well-mixed system, considering the concentrations of signaling molecules and the lifetime of binding events but not their spatial distribution (3, 8, 13, 15); as such, they would predict no dependence of the signaling activity on the spacing between antigens. In contrast, because the spatial distributions of LAT molecules can affect their propensity to form clusters, it is likely that our model would predict some dependence between the spatial distribution of pMHC-bound TCRs and signaling activity.

We therefore tested how our model responds to differing spatial arrangements of pMHCs. We ran simulations where a four-by-four grid of pMHCs was placed opposing the T cell so that TCRs could only bind and activate in those locations (Fig. 5*A*). We varied the 2D density of pMHCs over roughly three orders of magnitude by adjusting the inter-pMHC spacing, while keeping the number of pMHCs constant, and examined the effects on LAT clustering (Fig. 5 *B* and *C*). In contrast to other models, our simulations show that there is an intermediate spacing of pMHCs that is optimal for LAT cluster formation and T cell signaling (Fig. 5*C* and [Movies S12–S16](#)). At very low pMHC densities, each pMHC–TCR complex is isolated from others such that pLAT produced at one TCR is dephosphorylated before it can reach a cluster formed at another TCR (Fig. 5*D*). As the pMHC density increases, TCRs are able to cooperate, adding pLAT to clusters that were nucleated by other TCRs, allowing the cluster to grow larger than what could be produced by a single pMHC–TCR complex (Fig. 5*E*). However, if the pMHCs are brought too close together, then the TCRs become crowded, merging into what is effectively a single TCR that produces pLAT at a higher rate. This allows a cluster to form faster, but the cluster size is limited by the small area covered by the pMHCs (Fig. 5*F*). Thus, LAT condensation sets the spatial scales of TCR activation in addition to the temporal scales discussed earlier.

2D Protein Arrays Allow Precise Tuning of pMHC Spacing Independent of Dose. In order to test the prediction of optimal pMHC density, we developed an imaging assay to probe the relationship between antigen density and LAT clustering. As a platform for antigen presentation we used a 2D protein array (28) to place pMHCs at regular intervals (Fig. 6*A*). The arrays consist of two components in addition to the pMHC: the A component which is fused to the SpyCatcher protein (42), and the B component which is fused to green fluorescent protein (GFP). When mixed, the A and B components self-assemble into a hexagonal grid (Fig. 6*A*). By controlling the stoichiometry of the SpyTag–pMHC and SpyCatcher–A prior to assembly with component B, we can control the proportion of vertices of the array that present a pMHC, thus setting the average 2D density of pMHCs on the arrays. Furthermore, by quantifying stochastic variations in the sizes of arrays we are able to assess effects of variations in pMHC number, thus allowing us to independently assess the effects of pMHC spacing and number on TCR signaling.

As a model antigen, we presented the gp33–41 peptide from Lymphocytic Choriomeningitis Virus (LCMV) complexed to the

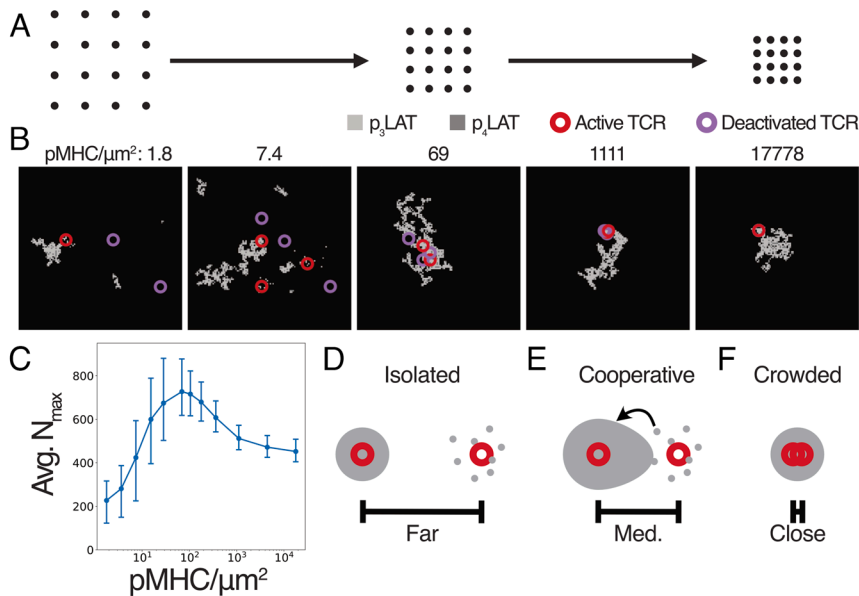


Fig. 5. Simulations predict an optimal pMHC spacing for LAT condensate formation and TCR signaling. Data from simulations with 16 fixed pMHCs at varying spacing, with WT LAT. 500 replicate simulations were run for each pMHC density. (A) Schematic of pMHC placement in simulations of varying antigen density at constant antigen number. (B) Snapshots from example simulations at different pMHC densities. Light gray squares represent p₃LAT and dark gray represent p₄LAT. Circles represent bound TCRs, red for active and purple for deactivated. Each snapshot represents a 3.47 × 3.47 μm square. (C) Mean N_{max} values for each pMHC density. Error bars show 25th and 75th percentiles of replicate simulations. (D–F) Cartoon representation of the underlying cause of optimal spacing. Large gray circles represent pLAT clusters, small gray circles represent individual pLAT molecules, and red circles represent TCRs. (D) At low pMHC density, pMHC-bound TCRs are isolated, preventing pLAT produced at one TCR from augmenting a condensate at the neighboring TCR. (E) At intermediate pMHC density pLAT produced at one pMHC-bound TCR can add to a condensate nucleated at a neighboring TCR. (F) At high pMHC density, neighboring pMHC-bound TCRs are crowded, limiting the area over which a condensate can form.

murine class I MHC, H-2D(b) (43). We used these ligands to stimulate a Jurkat T cell line expressing the cognate P14 transgenic TCR and the CD8 coreceptor. This cell line has been shown to give rise to robust downstream signaling when stimulated conventionally (9).

After the arrays were assembled, we seeded them onto a glass imaging surface and plated the P14 Jurkat cells on top of them. After a brief stimulation, we fixed the cells and stained them for the TCR subunit phospho-CD3ζ (pCD3ζ) and pLAT (Fig. 6 B and C). Each array produced a bright GFP spot in the image which we used to locate the regions of the image where arrays overlapped cells. We additionally calibrated our measurements of GFP brightness in order to be able to count the number of GFP molecules and, by extension, the number of pMHCs present in each array (SI Appendix, Fig. S4) (44). Using these values, along with several other measurements, we filtered the arrays to remove aggregates and imaging noise, yielding a set of high quality arrays that we used in all downstream analysis (SI Appendix, Fig. S5).

We first used the median phosphorylation signal in each array as a measure of the effectiveness of array stimulation (Fig. 6 D and E). These measurements showed a significant elevation of pCD3ζ and pLAT levels for arrays that have a high density of pMHC on them, while those with no pMHC did not induce any phosphorylation above background (Fig. 6 D and E). Additionally, larger arrays (higher GFP copy number) induced higher levels of phosphorylation (Fig. 6E). These results confirm that we were able to stimulate Jurkats with the arrays in a pMHC-dependent manner, and that phosphorylation is dependent on the number of pMHCs contacting the cell. We note that array-displayed pMHCs differ from those displayed on cell membranes in their TCR contact heights, as well as their ability to exclude membrane-associated proteins such as phosphatases. These kinds of differences have been shown to impact TCR signaling initiation (45, 46) and could affect the fit of the model to the resulting data because the model was adjusted to match data from membrane-bound pMHC stimulation. We therefore compare only general trends in these experiments with the model predictions instead of precise values.

Consistent with the differing biochemical mechanisms for activation of CD3ζ and LAT, the distributions of their phosphorylation levels show different shapes in response to pMHC stimulation (Fig. 6E). The pCD3ζ distribution shows a clear increase in its mode relative to the background distribution as the array size increases, consistent with CD3ζ phosphorylation occurring in proportion to

the number of pMHCs present. The pLAT distribution, on the other hand, shows a widening tail to the right without a major shift of the mode. This distribution is consistent with pLAT signals resulting from stochastic cluster nucleation in a fraction of cases that increases with pMHC number. These results are consistent with our model prediction that LAT signaling condensates nucleate only for a fraction of pMHCs (Fig. 3C), but can grow to large sizes that scale with the number of initiating TCR inputs (Fig. 4 G and H).

pMHC Arrays Reveal Optimal Antigen Spacing for LAT Condensation. After confirming the functionality of the 2D pMHC arrays, we tested whether varying pMHC density has an impact on downstream signaling. To do this we created arrays with pMHC density varying from 37.5 to 2,400 pMHC/μm² and measured the CD3ζ and LAT phosphorylation responses to each density. We first examined the relationship between array size and phosphorylation signal and found that, for all pMHC densities above zero, phosphorylation increased with increasing array size (SI Appendix, Fig. S6A). The slope of this relationship also increased with increasing pMHC density (SI Appendix, Fig. S6B). These results show increasing pMHC number results in a stronger downstream CD3ζ and LAT phosphorylation; more antigen results in a stronger signal.

After demonstrating that pMHC array stimulation produces the expected response to varying pMHC number, we next tested whether TCR signaling additionally varies with pMHC spacing. To compare arrays across all pMHC densities despite nonoverlapping distributions of pMHC number, we measured the activation efficiency for arrays of each density. This metric is defined as the slope of the line of best fit to the relationship between phosphorylation intensity and pMHC number (SI Appendix, Fig. S7), measuring the pY signal per pMHC at a given spacing. We observed a significant deviation from a flat line in response to pMHC density for LAT activation, efficiency, but not for CD3ζ (Fig. 6 F–H and SI Appendix, Fig. S8). This behavior is very similar to the behavior predicted by our model (Fig. 5). The phosphorylation of CD3ζ, which does not participate in LAT condensation, is not significantly impacted by pMHC density. Conversely, LAT phosphorylation is dependent on pMHC density, and requires an optimal density for maximal signaling. These experimental and simulated results further demonstrate that LAT condensation is central to the TCR signaling pathway. Thus, LAT condensation controls both the length and time scales required for optimal T cell activation.

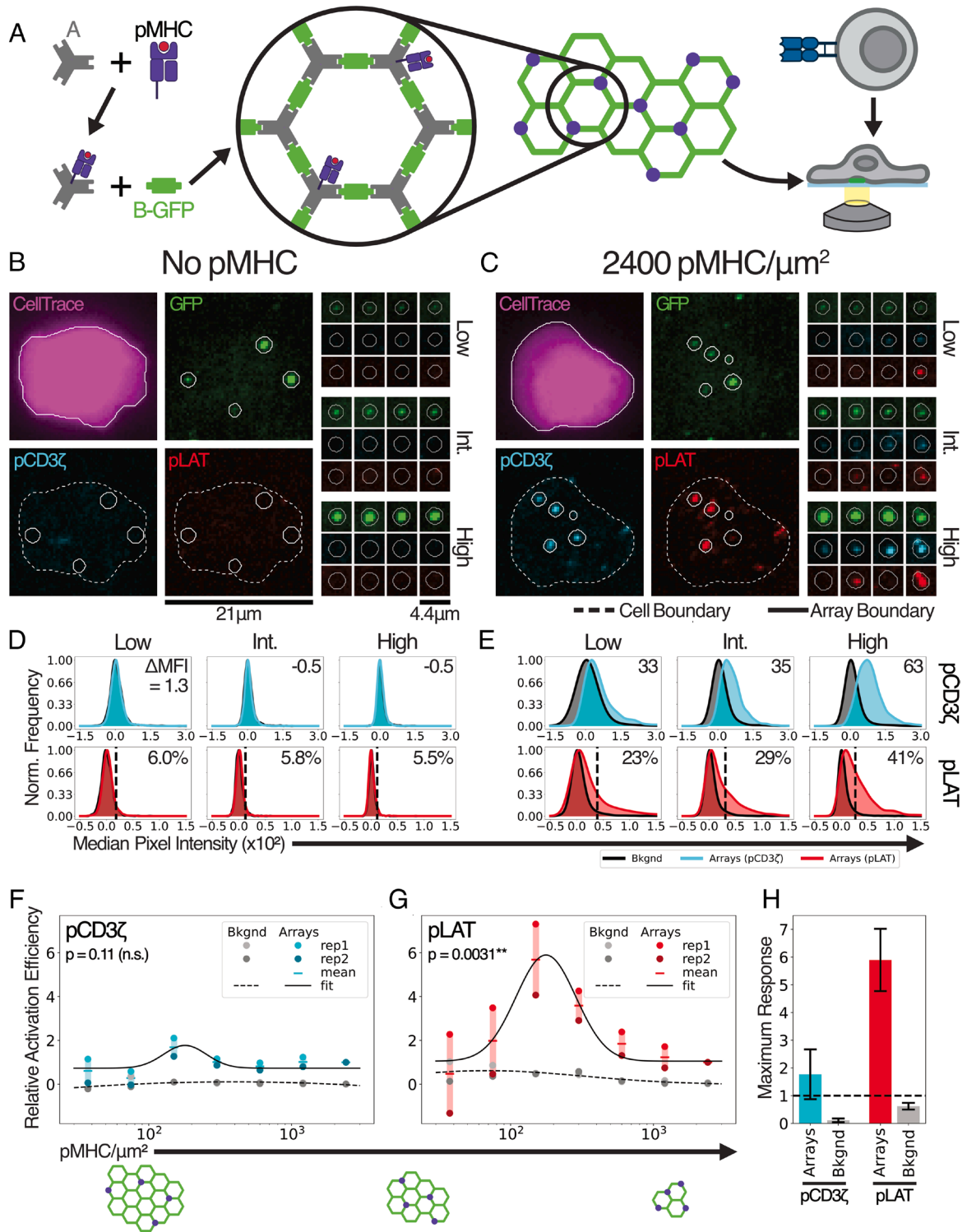


Fig. 6. Protein arrays for precise pMHC presentation reveal optimal pMHC spacing for pLAT condensate formation. (A) Illustration of the array assembly and imaging protocol. Components A and B are shown as gray triangles and green rectangles, respectively. The assembled array has a 31 nm distance between opposing edges of each hexagonal unit (28). (B and C) Example images of cells (purple) and arrays (green) that were fixed 5 min after interacting with blank (B) or pMHC-presenting arrays (C) showing the pCD3ζ (light blue) or pLAT (red) responses to pMHC array stimulation. Larger fields of view (Left) show a single representative cell interacting with arrays. Smaller fields of view (Right) show four representative arrays with either low (33rd percentile), intermediate (int.; 66th percentile), or high (100th percentile) GFP intensities. (D and E) Mode-normalized kernel density estimates for the distributions of median pCD3ζ (light blue, Top) or pLAT (red, Bottom) signal for arrays with low (Left; 0 to 33rd percentile) intermediate (Middle; 33rd to 66th percentile) or high (Right; 66th to 100th percentile) GFP intensities, compared to the same measurement in random locations (gray) for blank (D) or pMHC-presenting arrays (E). (F and G) Line plots showing CD3ζ (F) or LAT (G) activation efficiency as a function of pMHC density for arrays (colored) or background (gray). Activation efficiency is defined as the slope of the line of best fit for the relationship between integrated phosphorylation intensity and pMHC number. Data from two biological replicates (rep1 and rep2; filled circles) and their mean (bars) are shown, with each replicate independently normalized to the efficiency at 2,400 pMHC/μm². Black lines show a fit to a Gaussian curve for pooled data across replicates for arrays (solid lines) or background (dashed lines). P-values comparing the Gaussian fit of the array data to a flat line (SI Appendix, Fig. S8) are listed in each plot. P-values above 0.05 are marked with n.s., and those below 0.01 are marked with **. (H) Bar plots showing the maximal value of the fitted Gaussian for pCD3ζ and pLAT. Error bars indicate the SD derived from curve-fitting. The dashed line indicates a response value of 1, equivalent to no change relative to the highest pMHC density tested.

Discussion

Our results demonstrate that the dynamics of LAT phosphorylation, diffusion, and condensation downstream of the TCR can simultaneously give rise to sensitivity, selectivity, and dynamic range in T cell antigen sensing. While other signaling mechanisms can individually enhance these properties (3, 5, 8, 13, 15, 16, 20), it has not been clear how these mechanisms can simultaneously balance the opposing constraints imposed by all three of these properties. Through its inherent physical properties, the LAT nucleation-condensation process enables the TCR signaling pathway to simultaneously realize all these features in a single signaling step. Cluster growth following nucleation provides a strong positive feedback mechanism that can amplify even a single pMHC binding event into a large signaling response. The resulting cluster grows in proportion to the amount of available pLAT, imparting the system with a wide dynamic range in its response to pMHC levels. Finally, the inherent delay in cluster nucleation filters out weak pMHC binding events, enabling proofreading and selective responses to long-lasting pMHC–TCR binding events.

Our results also reveal a strong dependence of T cell signaling on the spatial distribution of antigens. The length scale of the pLAT gradient under an pMHC-bound TCR sets an optimal antigen spacing for LAT cluster growth. This optimal antigen spacing was predicted by our model and confirmed in our experiments, and aligns well with results from prior work using DNA origami (45, 47) or nanofabrication (48) techniques to specify the spatial arrangement of TCR ligands. Both of these methods allow precise control of the grouping of TCR ligands independent of their overall abundance. Across all these studies, there was a clear effect of ligand arrangement on TCR signaling even at a fixed overall ligand density, similar to our model's predictions. In future studies, it will be interesting to examine whether tuning ligand spacing can be a strategy for optimizing T cell signaling and effector responses, particularly in the context of immunotherapy.

Ultimately, LAT condensation will likely work together with other signaling and feedback mechanisms to specify the functional properties of TCR signaling. For instance, negative feedback loops initiated downstream of clustering may further improve selectivity (3, 5). Similarly, the inclusion of kinetic proofreading steps upstream of LAT phosphorylation could also improve selectivity. In future work, it will be important to analyze the relative roles and contributions of these distinct biochemical processes to T cell antigen sensing and signaling.

Our results point to a broader role for phase separation of signaling pathway components in shaping cellular responses across diverse physiological and pathological contexts. In T cells, phase separation provides an intuitive explanation for how these cells can detect threats with high selectivity and sensitivity for effective immune protection. It also provides insight into the mechanisms by which mutations in key TCR pathway components could alter antigen recognition and lead to autoimmune disease. More generally, phase-separation phenomena are being discovered in a wide range of biologically relevant pathways (38, 49), and understanding how they contribute to signaling outcomes in these contexts could lead to valuable insights in many areas. Our model provides a framework to do exactly that by making it possible to explicitly model the contributions of phase-separation to cellular signaling networks.

Methods

Computational Model. Our computational model is based on a 2D square grid representing the inner leaflet of the plasma membrane. We chose to use a grid spacing of 30 nm to approximately match the space a single molecule of LAT

occupies in the densest LAT clusters observed experimentally. Within this grid, TCRs and pLAT molecules are modeled as occupying a single grid square to the exclusion of molecules of the same type. All other molecules are not present in the model, and their effects are modeled implicitly in the behavior of the TCRs and pLAT molecules. Each timestep of the model proceeds through the following steps:

1. TCR diffusion
2. pLAT dephosphorylation (CD45 activity)
3. TCR–pMHC binding and activation
4. LAT phosphorylation (ZAP70 activity)
5. pLAT diffusion
6. pLAT–pLAT binding (via Grb2, SOS, and PLC γ)

These steps are repeated for the desired number of time steps (for a total of 2 min of simulated time). The length of the time step is set to 125 μ s (unless otherwise indicated) so that the probability that any molecule would take more than one action within each step of the simulation is negligible. Further details of each step are outlined in the *SI Appendix, Modeling Appendix*.

Analysis of Simulation Results. The output of each simulation was analyzed to determine two key values:

1. N_{\max} : The maximum number of clustered molecules. This was defined as the maximal value of the number of molecules in clusters of size 50 or greater over the course of the simulation.
2. τ_{clust} : The time at which the first cluster formed in the simulation. In the main text and *SI Appendix, Figs. S1 and S3*, this was defined as the earliest time point at which the largest cluster in the simulation contained at least 50 molecules. In *SI Appendix, Fig. S2 A and C*, the minimum cluster size was varied from 5 to 50 molecules. In *SI Appendix, Fig. S2 B, D, and E*, the definition was the time at which the first period of sustained (duration $\geq D$) and rapid (growth rate $\geq R$) began, for varying values of D and R . For any definition of τ_{clust} simulations that never meet the defined criteria were ignored.

For each group of replicate simulations, the fraction of simulations achieving a cluster (F_{clust}) was calculated as the fraction of simulations with $N_{\max} \geq 50$. All simulation results presented here are derived from $F_{\text{clust}} N_{\max}$ or τ_{clust} .

Array Component Purification. SpyCatcher-fused component A (A-SC) and GFP-fused cyclic component B (B-c-GFP) were expressed in *Escherichia coli* as previously described (28). *E. coli* cell pellets were resuspended in TBS supplemented with 5% (w/v) glycerol (TBSG), 1 mM PMSF, and 0.7 U/mL RNase A and lysed by sonication. Lysate was clarified by centrifugation at 14,000 \times g for 30 min and His-tagged array components were purified from the soluble fraction by Ni affinity chromatography in TBSG with either 40 mM imidazole (wash) or 500 mM imidazole (elution). Eluted components were further purified by size exclusion chromatography on a Superose 6 Increase 10/300 G/L column (Cytiva 29091596) to select the components that assembled into the correct oligomeric state.

Array Assembly. Refolded SpyTag-fused H-2D(b) bound to the LCMV gp33 peptide (KAVYNFATM) (ST-pMHC) was provided by the NIH Tetramer Facility. Varying molar ratios of ST-pMHC and purified A-SC from 1:3 to 1:192 (ST-pMHC:A-SC) were mixed and incubated overnight at 4 $^{\circ}$ C to allow formation of the SpyCatcher-SpyTag bond. The resulting A-pMHC and an unreacted A-SC control were then each mixed with B-c-GFP and diluted to a final concentration of 5 μ M A-SC and 2.5 μ M B-c-GFP in TBSG with 500 mM imidazole. The final mixture was allowed to assemble overnight at 4 $^{\circ}$ C, protected from light. Assembled arrays were separated from free components by centrifugation at 5,000 \times g for 5 min. After aspirating the supernatant, the pelleted arrays were resuspended in TBSG with 500 mM imidazole to their original volumes before aspirating.

Cell Line. The Jurkat cells used in these experiments were provided by Matthew Wither. They were produced by transducing a TCR β -knockout Jurkat line with two lentiviral vectors. The first vector expressed the α and β chains of the P14 TCR (fully murine sequences) under the same promoter, separated by a P2A linker. The second vector expressed CD8 α and CD8 β (fully murine sequences), again under the same promoter, separated by a P2A linker. A single clone was selected from the doubly transduced cells and expanded for imaging experiments.

Cell Culture. P14 Jurkat cells grown in Roswell Park Memorial Institute 1640 medium (Gibco 11835-030) supplemented with 10% fetal bovine serum (VWR 89510-186), 10 mM HEPES (Gibco 15630-080), 1 mM sodium pyruvate (Gibco 11360-070), and 1 × Pen/Strep/Glu (Gibco 10378-016) (T cell media). Cells were stored as 500 μ L aliquots at 5 M/mL in T cell media with 5% dimethyl sulfoxide in a liquid nitrogen dewar. Four days prior to imaging, cells were thawed, washed with 2.5 mL of T cell media, plated in 5 mL T cell media in a 6 cm dish and incubated for 2 d at 37 °C and 5% CO₂. After 2 d cells were counted and diluted to 100 k cells/mL in T cell media and incubated for another 2 d.

Jurkat Stimulation and Staining. All stimulation and staining was performed in a 96-well black-sided glass-bottom plate (MatTek PBK96G-1.5-5-F). The plate was first coated with a mixture of anti-GFP (100× dilution; MBL Life Science 598), anti-LFA1 (10 ng/ μ L; BioLegend 301202), and retronectin (20 ng/ μ L; Takara T100B) in PBS overnight at 4 °C. After coating, the plate was blocked in 1% casein (Sigma Aldrich C8654) for 1 h at 37 °C and washed three times with PBS. Each well of the plate was then coated with 50 μ L of a 2,000× dilution of assembled arrays in TBSG with 500 mM imidazole. The plate was centrifuged at 100× g for 5 min to improve array coating and washed three times with PBS with 0.1% CHAPS, and three times with PBS to remove any arrays and unassembled components not firmly attached. P14 Jurkats were seeded into the plate at 35 k cells/well and centrifuged at 100× g for 1 min to induce contact with the arrays. After 5 min of incubation at room temperature (including the 1 min centrifugation) cells were fixed with BD fixation buffer (BD Biosciences 51-2090KZ) for 30 min at room temperature. Fixed cells were permeabilized and blocked with a 1× BD wash/perm buffer (BD Biosciences 51-2091KZ; diluted from 10× in Fc blocking buffer) for 15 min at room temperature, protected from light. Cells were then washed twice with 1× BD wash/perm buffer diluted in PBS, and stained overnight at 4 °C, protected from light, with 50 μ L/well of PE-anti-pLAT (BD Biosciences 558487; 5× dilution) and AF647-anti-pCD3 ζ (Abcam ab237452; 100× dilution) in 1× BD wash/perm buffer diluted with PBS. Staining solution was removed with two washes with BD perm/wash diluted in PBS and one with PBS. Cells were then stained with 100 μ L of 5 μ M CellTrace Violet (Invitrogen C34557) in PBS for 20 min at room temperature, protected from light. Excess CellTrace was removed with three washes in PBS, and cells were left in PBS for imaging. All washes and buffer changes were performed with 100 μ L per well unless otherwise listed and all liquids were added gently to avoid dislodging the cells from the glass surface.

Imaging. Images of fixed and stained cells were acquired on a Leica DMI8 with a spinning disc confocal, hardware autofocus, and a 63× (0.75 NA) glycerol objective. At each position, a z-stack of six slices separated by 200 nm, centered on the z-coordinate of the arrays was acquired. Images of cells (DIC, 100 ms exposure), CellTrace (405 Ex, 440/40 Em, 500 ms exposure), arrays/GFP (470 Ex; 510/50 Em, 900 ms exposure), PE-anti-pLAT (555 Ex, 600/50 Em, 200 ms exposure), and AF647-anti-pCD3 ζ (640 Ex, 700/75 Em, 900 ms exposure) were acquired at each slice using an LDI-7 from 89North at 50% power.

Image Processing. Images were processed using a custom MATLAB script to extract information about the CD3 ζ and LAT phosphorylation in areas where cells came in contact with pMHC arrays. First, a segmentation of the cells was determined from the CellTrace stain, including dimmer regions containing thin regions of cytoplasm in contact with the glass surface. Next, a segmentation of the arrays as determined from the GFP signal in a manner that allows detection of both very bright and very

dim arrays. Finally, the total or median fluorescence intensity in each channel (with the local background in a small ring around the array subtracted from each pixel) was calculated for each region where the two segmentations overlapped. As an image-internal control, the shape of each overlapping region was extracted and placed at a random location within a cell in the same image and the same total fluorescence quantification was made in that region.

GFP Counting. To estimate the number of GFP molecules present in an array from its total intensity, we used particles with known GFP copy number to calibrate our imaging protocol. Nanocages with either 60 or 120 GFP copies attached (44) were coated onto the glass imaging surface and fixed using the same protocol as the arrays. GFP nanocage images were segmented and quantified using the same custom scripts as the array images and the average total intensity for all segmented nanocages was calculated for each GFP copy number. A linear fit to these data allows interconversion between total GFP fluorescence intensity and GFP copy number (*SI Appendix, Fig. S4*).

Statistical Analysis of Imaging Data. To determine whether the optimal value of pMHC density observed on our imaging experiments was statistically significant, we compared two fits to the relative activation efficiency data. The first fit was a simple flat line, representing the null hypothesis that pMHC density does not impact activation efficiency. The second was a Gaussian with four parameters: amplitude, mean, SD, and baseline, representing the hypothesis that there is an optimal spacing. The Gaussian was constrained to have a SD greater than half the spacing between adjacent data points and a baseline above -3 (a value near, but lower than the lowest value in the dataset) in order to avoid overfitting to noisy data. The two fits were compared using the F-test to obtain a *P*-value for the significance of the improvement in the fit gained by fitting the Gaussian instead of the flat line. We also calculated the maximum height of the Gaussian fit (the sum of the amplitude and the baseline) as a measure of the effect size of pMHC spacing.

Data, Materials, and Software Availability. Summarized simulation and imaging data, and the code used to run simulations and analyze simulation and imaging data have been uploaded to the Kueh lab github (https://github.com/kuehlab/LAT-clustering_White-et-al-2025) (50).

ACKNOWLEDGMENTS. We thank members of the Kueh lab, in particular Morgan Bean, for discussion and feedback, Matthew Wither for providing the P14 Jurkat cell line. We also thank Tony Cooke (previously with Leica Microsystems) for microscope setup and support, and the NIH Tetramer Core Facility for providing SpyTag-pMHC monomers. We also thank Lenore Cowen for providing additional computing resources. This study was funded by an NIH National Institute of Biomedical Imaging and Bioengineering Trailblazer Award (R21EB027327, H.Y.K.), two NIH R01 grants (R01CA282512 and R01CA282512, to H.Y.K.), a Bill and Melinda Gates Foundation grant (INV-010680, D.B.), and an NIH National Institute of Allergy and Infectious Diseases grant (P01AI091580, J.T.G.). Portions of the paper were developed from the thesis of W.L.W.

Author affiliations: ^aDepartment of Bioengineering, University of Washington, Seattle, WA 98195; ^bInstitute for Protein Design, University of Washington, Seattle, WA 98195; ^cDepartment of Chemistry, University of California Berkeley, Berkeley, CA 94720; ^dInstitute for Digital Molecular Analytics and Science, Nanyang Technological University, Singapore 636921, Singapore; ^eDepartment of Biochemistry, University of Washington, Seattle, WA 98195; ^fHHMI, Seattle, WA 98195; and ^gInstitute for Stem Cell and Regenerative Medicine, University of Washington, Seattle, WA 98109

1. P. A. van der Merwe, O. Dushek, Mechanisms for T cell receptor triggering. *Nat. Rev. Immunol.* **11**, 47–55 (2011).
2. J. A. Siller-Farfán, O. Dushek, Molecular mechanisms of T cell sensitivity to antigen. *Immunol. Rev.* **285**, 194–205 (2018).
3. P. François, G. Voisinne, E. Siggia, G. Altan-Bonnet, M. Vergassola, Phenotypic model for early T-cell activation displaying sensitivity, specificity, and antagonism. *Proc. Natl. Acad. Sci. U.S.A.* **110**, E888–897 (2013).
4. A. K. Chakraborty, A. Weiss, Insights into the initiation of TCR signaling. *Nat. Immunol.* **15**, 798–807.
5. G. Altan-Bonnet, R. N. Germain, Modeling T cell antigen discrimination based on feedback control of digital ERK responses. *PLoS Biol.* **3**, e356 (2005).
6. A. C. Richard *et al.*, T cell cytolytic capacity is independent of initial stimulation strength. *Nat. Immunol.* **19**, 849–858 (2018).
7. C. Wülfing *et al.*, Kinetics and extent of T cell activation as measured with the calcium signal. *J. Exp. Med.* **185**, 1815–1825 (1997).
8. M. Lever *et al.*, Architecture of a minimal signaling pathway explains the T-cell response to a 1 million-fold variation in antigen affinity and dose. *Proc. Natl. Acad. Sci. U.S.A.* **113**, E6630–E6638 (2016).
9. M. J. Wither *et al.*, Antigen perception in T cells by long-term Erk and NFAT signaling dynamics. *Proc. Natl. Acad. Sci. U.S.A.* **120**, e2308366120 (2023).
10. R. J. Brownlie, R. Zamoyska, T cell receptor signaling networks: Branched, diversified and bounded. *Nat. Rev. Immunol.* **13**, 257–269 (2013).
11. A. H. Courtney, W.-L. Lo, A. Weiss, TCR signaling: Mechanisms of initiation and propagation. *Trends Biochem. Sci.* **43**, 108–123 (2018).
12. V. Di Bartolo *et al.*, Tyrosine 319, a newly identified phosphorylation site of ZAP-70, plays a critical role in T cell antigen receptor signaling. *J. Biol. Chem.* **274**, 6285–6294 (1999).
13. T. W. McKeithan, Kinetic proofreading in T-cell receptor signal transduction. *Proc. Natl. Acad. Sci. U.S.A.* **92**, 5042–5046 (1995).
14. D. K. Tischer, O. D. Weiner, Light-based tuning of ligand half-life supports kinetic proofreading model of T cell signaling. *Elife* **8**, e42498 (2019).

15. R. S. Ganti *et al.*, How the T cell signaling network processes information to discriminate between self and agonist ligands. *Proc. Natl. Acad. Sci. U.S.A.* **117**, 26020–26030 (2020).
16. T. Lipniacki, B. Hat, J. R. Faeder, W. S. Hlavacek, Stochastic effects and bistability in T cell receptor signaling. *J. Theor. Biol.* **254**, 110–122 (2008).
17. J. Das *et al.*, Digital signaling and hysteresis characterize Ras activation in lymphoid cells. *Cell* **136**, 337–351 (2009).
18. U. Alon, *An Introduction to Systems Biology: Design Principles of Biological Circuits* (Chapman and Hall/CRC, New York, 2006).
19. J. J. Y. Lin *et al.*, Mapping the stochastic sequence of individual ligand-receptor binding events to cellular activation: T cells act on the rare events. *Sci. Signal.* **12**, eaat8715 (2019).
20. D. Kirby, A. Zilman, Proofreading does not result in more reliable ligand discrimination in receptor signaling due to its inherent stochasticity. *Proc. Natl. Acad. Sci. U.S.A.* **120**, e2212795120 (2023).
21. X. Su *et al.*, Phase separation of signaling molecules promotes T cell receptor signal transduction. *Science* **352**, 595–599 (2016).
22. L. Zeng, I. Palaia, A. Sarić, X. Su, PLC γ 1 promotes phase separation of T cell signaling components. *J. Cell Biol.* **220**, e202009154 (2021).
23. A. Nag, M. I. Monine, J. R. Faeder, B. Goldstein, Aggregation of membrane proteins by cytosolic cross-linkers: Theory and simulation of the LAT-Grb2-SOS1 system. *Biophys. J.* **96**, 2604–2623 (2009).
24. W. Y. C. Huang *et al.*, A molecular assembly phase transition and kinetic proofreading modulate Ras activation by SOS. *Science* **363**, 1098–1103 (2019).
25. J. Yi, L. Balagopalan, T. Nguyen, K. M. McIntire, L. E. Samelson, TCR microclusters form spatially segregated domains and sequentially assemble in calcium-dependent kinetic steps. *Nat. Commun.* **10**, 277 (2019).
26. S. Sun, T. GrandPre, D. T. Limmer, J. T. Groves, Kinetic frustration by limited bond availability controls the LAT protein condensation phase transition on membranes. *Sci. Adv.* **8**, eabo5295 (2022).
27. D. B. McAfee *et al.*, Discrete LAT condensates encode antigen information from single pMHC:TCR binding events. *Nat. Commun.* **13**, 7446 (2022).
28. A. J. Ben-Sasson *et al.*, Design of biologically active binary protein 2D materials. *Nature* **589**, 468–473 (2021).
29. W.-L. Lo *et al.*, Slow phosphorylation of a tyrosine residue in LAT optimizes T cell ligand discrimination. *Nat. Immunol.* **20**, 1481–1493 (2019).
30. W.-L. Lo *et al.*, A single-amino acid substitution in the adaptor LAT accelerates TCR proofreading kinetics and alters T-cell selection, maintenance and function. *Nat. Immunol.* **24**, 676–689 (2023).
31. D. M. Brittain, J. P. Town, O. D. Weiner, Progressive enhancement of kinetic proofreading in T cell antigen discrimination from receptor activation to DAG generation. *Elife* **11**, e75263 (2022).
32. O. S. Yousefi *et al.*, Optogenetic control shows that kinetic proofreading regulates the activity of the T cell receptor. *Elife* **8**, e42475 (2019).
33. W. Zhang *et al.*, Association of Grb2, Gads, and phospholipase C- γ 1 with phosphorylated LAT tyrosine residues: Effect of LAT tyrosine mutations on T cell antigen receptor-mediated signaling. *J. Biol. Chem.* **275**, 23355–23361 (2000).
34. N. H. Shah *et al.*, An electrostatic selection mechanism controls sequential kinase signaling downstream of the T cell receptor. *Elife* **5**, e20105 (2016).
35. S. Cho *et al.*, Structural basis for differential recognition of tyrosine-phosphorylated sites in the linker for activation of T cells (LAT) by the adaptor Gads. *EMBO J.* **23**, 1441–1451 (2004).
36. A. H. Courtney *et al.*, CD45 functions as a signaling gatekeeper in T cells. *Sci. Signal.* **12**, eaaw8151 (2019).
37. J. R. James, R. D. Vale, Biophysical mechanism of T-cell receptor triggering in a reconstituted system. *Nature* **487**, 64–69 (2012).
38. L. B. Case, J. A. Ditlev, M. K. Rosen, Regulation of transmembrane signaling by phase separation. *Annu. Rev. Biophys.* **48**, 465–494 (2019).
39. A. A. Hyman, C. A. Weber, F. Jülicher, Liquid-liquid phase separation in biology. *Annu. Rev. Cell Dev. Biol.* **30**, 39–58 (2014).
40. C. L. Sommers *et al.*, A LAT mutation that inhibits T cell development yet induces lymphoproliferation. *Science* **296**, 2040–2043 (2002).
41. R. A. Gottschalk *et al.*, Distinct influences of peptide-MHC quality and quantity on in vivo T-cell responses. *Proc. Natl. Acad. Sci. U.S.A.* **109**, 881–886 (2012).
42. B. Zakeri *et al.*, Peptide tag forming a rapid covalent bond to a protein, through engineering a bacterial adhesin. *Proc. Natl. Acad. Sci. U.S.A.* **109**, E690–E697 (2012).
43. H. Pircher *et al.*, Molecular analysis of the antigen receptor of virus-specific cytotoxic T cells and identification of a new V α family. *Eur. J. Immunol.* **17**, 1843–1846 (1987).
44. Y. Hsia *et al.*, Design of a hyperstable 60-subunit protein icosahedron. *Nature* **535**, 136–139 (2016).
45. J. Hellmeier *et al.*, DNA origami demonstrates the unique stimulatory power of single pMHCs as T cell antigens. *Proc. Natl. Acad. Sci. U.S.A.* **118**, e2016857118 (2021).
46. K. B. Wilhelm *et al.*, Height, but not binding epitope, affects the potency of synthetic TCR agonists. *Biophys. J.* **120**, 3869–3880 (2021).
47. R. Dong *et al.*, DNA origami patterning of synthetic T cell receptors reveals spatial control of the sensitivity and kinetics of signal activation. *Proc. Natl. Acad. Sci. U.S.A.* **118**, e2109057118 (2021).
48. H. Cai *et al.*, Full control of ligand positioning reveals spatial thresholds for T cell receptor triggering. *Nat. Nanotechnol.* **13**, 610–617 (2018).
49. R. S. Lach *et al.*, Nucleation of the destruction complex on the centrosome accelerates degradation of β -catenin and regulates Wnt signal transmission. *Proc. Natl. Acad. Sci. U.S.A.* **119**, e2204688119 (2022).
50. W. L. White, H. Y. Kueh, LAT-Clustering_White-et-al-2025. GitHub. https://github.com/kuehlab/LAT-clustering_White-et-al-2025. Accessed 11 May 2025.